

Active Brownian particles simulated in molecular dynamics

Liya Wang(王丽雅), Xinpeng Xu(徐新鹏), Zhigang Li(李志刚), Tiezheng Qian(钱铁铮)

Citation: Chin. Phys. B . 2020, 29(9): 090501 . **doi:** 10.1088/1674-1056/aba60d
Journal homepage: http://cpb.iphy.ac.cn; http://iopscience.iop.org/cpb

What follows is a list of articles you may be interested in

Ergodicity recovery of random walk in heterogeneous disordered media

Liang Luo(罗亮), Ming Yi(易鸣)
Chin. Phys. B . 2020, 29(5): 050503 . **doi:** 10.1088/1674-1056/ab8212

A novel image encryption scheme based on Kepler's third law and random Hadamard transform

Yu-Ling Luo(罗玉玲), Rong-Long Zhou(周戎龙), Jun-Xiu Liu(刘俊秀), Sen-Hui Qiu(丘森辉), Yi Cao(曹弋)
Chin. Phys. B . 2017, 26(12): 120504 . **doi:** 10.1088/1674-1056/26/12/120504

Collective transport of Lennard–Jones particles through one-dimensional periodic potentials

Jian-hui He(何健辉), Jia-le Wen(温家乐), Pei-rong Chen(陈沛荣), Dong-qin Zheng(郑冬琴), Wei-rong Zhong(钟伟荣)
Chin. Phys. B . 2017, 26(7): 070502 . **doi:** 10.1088/1674-1056/26/7/070502

Pattern dynamics of network-organized system with cross-diffusion

Qianqian Zheng(郑前前), Zhijie Wang(王直杰), Jianwei Shen(申建伟)
Chin. Phys. B . 2017, 26(2): 020501 . **doi:** 10.1088/1674-1056/26/2/020501

Uphill anomalous transport in a deterministic system with speed-dependent friction coefficient

Wei Guo(郭伟), Lu-Chun Du(杜鲁春), Zhen-Zhen Liu(刘真真), Hai Yang(杨海), Dong-Cheng Mei(梅冬成)
Chin. Phys. B . 2017, 26(1): 010502 . **doi:** 10.1088/1674-1056/26/1/010502

Active Brownian particles simulated in molecular dynamics*

Liya Wang(王丽雅)[1,4], Xinpeng Xu(徐新鹏)[2], Zhigang Li(李志刚)[3], and Tiezheng Qian(钱铁铮)[4,†]

[1] *Faulty of Civil Engineering and Mechanics, Jiangsu University, Zhenjiang* 212013, *China*
[2] *Faculty of Physics, Guangdong-Technion - Israel Institute of Technology, Shantou* 515063, *China*
[3] *Department of Mechanical and Aerospace Engineering, Hong Kong University of Science and Technology, Hong Kong, China*
[4] *Department of Mathematics, Hong Kong University of Science and Technology, Hong Kong, China*

(Received 25 May 2020; revised manuscript received 22 June 2020; accepted manuscript online 15 July 2020)

In the numerical studies of active particles, models consisting of a solid body and a fluid body have been well established and widely used. In this work, such an active Brownian particle (ABP) is realized in molecular dynamics (MD) simulations. Immersed in a fluid, each ABP consists of a head particle and a spherical phantom region of fluid where the flagellum of a microswimmer takes effect. Quantitative control over the orientational persistence time is achieved via an external stochastic dynamics. This control makes it possible to validate ABP's diffusion property in a wide range of particle activity. In molecular description, the axial velocity of ABP exhibits a Gaussian distribution. Its mean value defines the active velocity which increases with the active force linearly, but shows no dependence on the rotational diffusion coefficient. For the active diffusion coefficient measured in free space, it shows semi-quantitative agreement with the analytical result predicted by a minimal ABP model. Furthermore, the active diffusion coefficient is also calculated by performing a quantitative analysis on the ABP's distribution along x axis in a confinement potential. Comparing the active diffusion coefficients in the above two cases (in free space and in confinement), the validity of the ABP modeling implemented in MD simulations is confirmed. Possible reasons for the small deviation between the two diffusion coefficients are also discussed.

Keywords: active Brownian particle, diffusion, confinement, boundary

PACS: 05.40.–a, 05.40.Jc, 83.10.Rs **DOI:** 10.1088/1674-1056/aba60d

1. Introduction

Active particles are self-propelled, capable of converting energy from the environment or the food into directed motion.[1–4] Ubiquitous examples include bacteria,[5–8] motile cells,[9–11] and artificial Janus particles.[12,13] Due to the constant energy supply and consumption, active particles are nonequilibrium by nature, making active suspensions intrinsically different from their passive counterparts.[7,14,15]

Active particles swimming at small length scale are governed by low Reynolds number hydrodynamics dominated by viscous damping.[16] For hydrodynamically interacting active particles, the fluid flow generated by one swimmer inevitably influences the motion of nearby swimmers. It has been generally accepted that hydrodynamic interactions play an important role in the dynamics of collective phenomena.[17–19] In addition, thermal Brownian noise originating from collisions with fluid particles also affects the motion of active particles significantly. In this sense, molecular dynamics (MD) simulations have the unique advantage in simulating active dynamics as both hydrodynamic interactions and thermal noise are naturally included.

The hydrodynamic flow induced by the activity of a microswimmer is usually described by using a force dipole.[3,19–21] Investigations of flagellated swimmers, e.g., *Escherichia coli* bacteria and *Chlamydomonas reinhardtii* algae, have confirmed this picture.[18,20–23] To model the motion of flagellated swimmers, flagellum is usually not explicitly described. Instead, a fluid body with active force exerted is introduced in the active particle modeling to incorporate the effect of a rotating flagellum. These models consisting of a solid body and a forced fluid region have been well established and widely used. Recently, the influences of particle shape anisotropy and hydrodynamic interactions have been investigated using the lattice-Boltzmann simulation.[24] In the fluid particle dynamics method, a "phantom" spherical particle is used to model the effect of a rotating flagellum.[19] In our MD simulations presented here, a spherical phantom region is introduced to an active particle, with the fluid particles in this region being subjected to the force exerted by the flagellum. The force dipole driving an active particle is formed by a pair of active forces, one exerted on its solid body and the other on the phantom region of fluid. As a result, the active particle can be modeled as a pusher or a puller depending on how the active forces are directed.

With hydrodynamic effects completely neglected, microswimmers are commonly described by a minimal model for active Brownian particles (ABPs),[2–4] which can effectively capture various fundamental features of microswimmers: overdamped dynamics, self-propelled motion, and thermal noises acting on the translational and rotational degrees

*Project supported by Hong Kong RGC CRF, China (Grant No. C1018-17G), GRF, China (Grant No. 16228216), and Jiangsu University Foundation (Grant No. 20JDG20).

†Corresponding author. E-mail: maqian@ust.hk

© 2020 Chinese Physical Society and IOP Publishing Ltd

of freedom. In particular, spherical ABPs are widely used because of their simple shape.[12,25,26] It has been well established that the shapes of active and passive particles have significant effects on their dynamics,[27–30] but this is beyond the scope of the present work. In the minimal model for ABPs, one of the basic assumptions is the constant self-propulsion speed of each particle. However, this is not always the case, especially in a dense suspension of interacting active particles.[31–33] In our MD simulations, the ABP is simulated as a pusher that is driven by a force dipole.

To the best of our knowledge, this is the first effort in which an ABP consisting of a solid body and a fluid body is realized in MD simulations. Before directly applying this model to the collective dynamics, some quantitative validations are necessary, given the presence of additional complexities in the molecular description. For this purpose, the dilute ABP suspension is adopted and the many-body behaviors induced by the hydrodynamic interactions are not within the scope of this work. A notable feature of ABP is that its active diffusion coefficient D_{A} can be roughly estimated as the product of the orientational persistence time τ_{r} and the square of active velocity v_{A}. In particular, $D_{\mathrm{A}} = v_{\mathrm{A}}^2\tau_{\mathrm{r}}/3$ is quantitatively predicted in the commonly used minimal ABP model.[3] In our MD simulations, we simulate ABPs' diffusion in free space and investigate to what extent this relation remains valid. Moreover, the active diffusion coefficient is measured when the ABP is placed in a confinement potential. Through the comparison between the diffusion coefficients measured in free space and in confinement, it is shown that the ABP model consisting of a solid body and a fluid body implemented in MD simulations is able to grasp the salient features of the overdamped ABPs. For confined active particles, the typical bimodal distribution, i.e., the boundary accumulation effect, has been intensively studied due to its unique out-of-equilibrium nature.[13,34–41] Here in our MD simulations, a clear evolution from the Boltzmann-type distribution to bimodal distribution is also observed.

The paper is organized as follows. In Section 2, we elaborate on how to realize an ABP as a pusher in MD simulations. Based on the dumbbell model, a modified ABP model with quantitatively tunable rotational dynamics is implemented. We also show that the axial velocity of the ABP exhibits a Gaussian distribution. Its mean value is defined as the active velocity v_{A} which increases with the active force F_{A} linearly but shows no dependence on the rotational diffusion coefficient D_{r}. In Section 3, we investigate the diffusive motion of ABPs in free space. Our numerical results support the relation $D_{\mathrm{A}} \propto v_{\mathrm{A}}^2\tau_{\mathrm{r}}$, and reasons are presented for why the MD results deviate from the prediction of the minimal model. In Section 4, we simulate and analyze the distribution of ABPs in an isotropic harmonic potential. A clear evolution from the Boltzmann-type distribution to non-Boltzmann distribution is demonstrated, in agreement with previous theoretical and numerical results.[34–36] In addition, the active diffusion coefficient is also acquired by performing a quantitative analysis on the particle distribution along the x axis. In comparison with that measured in free space, a fairly good semi-quantitative agreement is obtained. The paper is concluded in Section 5.

2. Active Brownian particles in MD simulations

2.1. Simulation details

To investigate the ABP dynamics in a dilute suspension, MD simulations are carried out for three active particles placed in a cubic box, as shown in Fig. 1(a). The simulated system is composed of three active particles and a large number of fluid particles. In the present work, the ABP is realized and simulated as a pusher, which is schematically illustrated in Fig. 1(b). Each ABP consists a solid body and a fluid body. The solid body is made by a spherical particle representing the active particle's head. This spherical particle will also be called the head particle. The fluid body is made by a spherical phantom region of fluid that is centered at a position away from the head particle along a certain direction. The orientation of the active particle is represented by a unit vector $\boldsymbol{n}$ in the direction from the center of the phantom region to the center of the head particle. To realize the ABP as a pusher, a pair of active forces $F_{\mathrm{A}}\boldsymbol{n}$ and $-F_{\mathrm{A}}\boldsymbol{n}$ form a force dipole, and are applied on the head particle and the phantom region of fluid, respectively. Physically, there is a thin flagellar bundle that is attached to the head particle and exerts a force on the phantom region of fluid.

The fluid particles are spherical and interact with each other through the Lennard–Jones (LJ) potential

$$V_{\mathrm{LJ}}^{\mathrm{ff}}(r) = 4\varepsilon_{\mathrm{ff}}\left[\left(\frac{\sigma_{\mathrm{ff}}}{r}\right)^{12} - \left(\frac{\sigma_{\mathrm{ff}}}{r}\right)^{6}\right], \tag{1}$$

where r is the distance between particles, and $\varepsilon_{\mathrm{ff}}$ and σ_{ff} denote the energy and length scales, respectively. The interaction parameters for fluid and head particles are all taken from a MD work which investigated the axial dispersion of Brownian colloids in microfluidic channels.[42] All the results in this paper are to be presented in the reduced units, with length measured by σ_{ff}, energy by $\varepsilon_{\mathrm{ff}}$, mass by m_{f} which is the mass of each fluid particle, and time by $\tau_0 = \sqrt{m_{\mathrm{f}}\sigma_{\mathrm{ff}}^2/\varepsilon_{\mathrm{ff}}}$. The LJ potential between fluid particles is cut off at $r_{\mathrm{cut}}^{\mathrm{ff}} = 2.5\sigma_{\mathrm{ff}}$. In our simulations, the average number density of fluid particles is $\rho = 0.8\sigma_{\mathrm{ff}}^{-3}$. The interaction between head particles is modelled by using the purely repulsive Weeks–Chandler–Anderson (WCA) potential,[43] which is obtained from the standard LJ potential with a truncation at the minimum potential energy at the distance $2^{1/6}\sigma_{\mathrm{aa}}$ and an upward shift by

the energy ε_{aa}

$$V_{\mathrm{WCA}}^{\mathrm{aa}}(r)=\begin{cases}4\varepsilon_{\mathrm{aa}}\left[\left(\frac{\sigma_{\mathrm{aa}}}{r}\right)^{12}-\left(\frac{\sigma_{\mathrm{aa}}}{r}\right)^{6}\right]+\varepsilon_{\mathrm{aa}}, & r\leqslant 2^{1/6}\sigma_{\mathrm{aa}},\\ 0, & r>2^{1/6}\sigma_{\mathrm{aa}}.\end{cases} \quad (2)$$

A strong repulsion with the energy scale $\varepsilon_{aa}=10\varepsilon_{ff}$ is used for head particles and the corresponding length scale is $\sigma_{aa}=3\sigma_{ff}$. The mass of each head particle is $m_a=10.64m_f$.[42] The interaction between head and fluid particles is modeled by using another LJ potential with the energy scale $\varepsilon_{af}=\varepsilon_{ff}$ and length scale $\sigma_{af}=(\sigma_{aa}+\sigma_{ff})/2=2\sigma_{ff}$. This interaction is cut off at $r_{cut}^{af}=2.5\sigma_{af}$.

For each active particle, the center of the fluid phantom region is away from the center of the head particle by a fixed distance of $5\sigma_{ff}$. The radius of the phantom region is $2\sigma_{ff}$ and there are always about 27 fluid particles in this region with small fluctuation. In addition, the active force F_A exerted on the phantom region is equally divided by the fluid particles in the region.

MD simulations have been carried out using the LAMMPS package.[44] The equations of motion are integrated using Velocity-Verlet algorithm with a time step of $0.0025\tau_0$. Using a Langevin thermostat in an NVE ensemble, the temperature of the fluid is controlled at $1.5\varepsilon_{ff}/k_B$, with k_B being the Boltzmann constant. For the average number density of fluid particles $\rho=0.8\sigma_{ff}^{-3}$ used here, there are 108000 fluid particles placed in a simulation box measuring $L_x\times L_y\times L_z=51.3\sigma_{ff}\times 51.3\sigma_{ff}\times 51.3\sigma_{ff}$. Periodic boundary conditions are applied in all the three directions. As a result, the spherical phantom region of an active particle may fall into several parts at the boundaries. As shown in Fig. 1(a), the phantom region of one active particle is separated into four parts at the boundary lines.

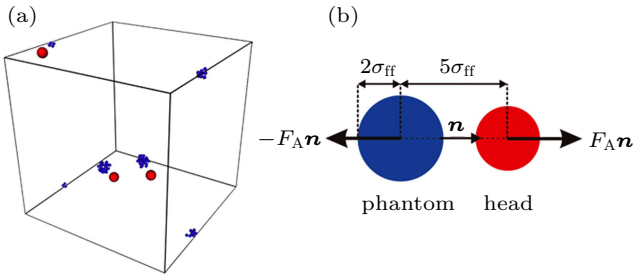


Fig. 1. (a) A snapshot of the simulation showing a dilute suspension of three active particles in the simulation box. The red particles are the head particles and the blue particles are the fluid particles in the phantom regions. Fluid particles out of the phantom regions are not shown here. Due to the periodic boundary conditions, the fluid body of one active particle is separated into four parts. (b) The ABP modeled in this work. A force dipole is exerted on the head particle and the phantom region of fluid to model a pusher.

2.2. Elementary aspects of active Brownian particles

Many different models have been proposed to describe the self-propelled motion of active particles.[38,45,46] A common feature of these models is that an active particle moves under the influence of certain directional control of stochastic nature. Different from a passive Brownian particle (PBP) with decoupled rotational and translational motions, the self-propelled motion of an ABP results in the coupling between rotational and translational degrees of freedom.[2]

2.2.1. Stochastic orientational dynamics

The dynamics of a spherical ABP is governed by the overdamped Langevin equations

$$\dot{\boldsymbol{r}}=v_A\boldsymbol{n}+\sqrt{2D_T}\boldsymbol{\xi}, \quad (3)$$

$$\dot{\boldsymbol{n}}=\sqrt{2D_r}\boldsymbol{n}\times\boldsymbol{\zeta}, \quad (4)$$

in which $\boldsymbol{r}$ is the particle position, $\boldsymbol{n}$ is the unit vector denoting the particle orientation, $v_A\boldsymbol{n}$ is the active velocity in the direction of $\boldsymbol{n}$ with v_A being the constant speed, D_T and D_r are the translational and rotational diffusion coefficients, respectively, and $\boldsymbol{\xi}$ and $\boldsymbol{\zeta}$ are three-dimensional translational and rotational Gaussian white noises, with each component having zero mean and unit variance.

In the present work, the orientational dynamics of an ABP, i.e., the time evolution of $\boldsymbol{n}$, is obtained by solving Eq. (4). This is accomplished as follows. Firstly, for a given value of D_r, equation (4) is numerically solved using a Python code to generate a time series of $\boldsymbol{n}$. Secondly, this series of $\boldsymbol{n}$ are used as the input to the MD simulation carried out by the LAMMPS package. The particle orientation $\boldsymbol{n}$ is read at each time step. Once $\boldsymbol{n}$ is given at a particular time step, the phantom region of fluid is located (relative to the head particle) and the force dipole along the particle orientation is then exerted, as illustrated in Fig. 1(b). As a result, the active particle is self-propelled in the direction of $\boldsymbol{n}$ amid the noises acting on the translational and rotational degrees of freedom.

In most ABP models, once the active force along the particle orientation is imposed, the rotational diffusion coefficient D_r is solely determined by thermal fluctuations. The dumbbell model in which the solid body is made by a head particle and a tail particle belongs to this category. The ABP model used here is in fact modified from the dumbbell model. Reasons why we perform the modification are as follows:

(i) The validation of ABP's diffusion properties needs to be performed in a wide range of activity conditions. However, the activity, i.e., the orientational persistence time of the dumbbell model, is fixed for a certain suspension system. Hence, we discard the tail particle and control the rotational dynamics via Eq. (4).

(ii) This control enables the orientational dynamics of ABP to be quantitatively tunable. Theoretically, any D_r value can be incorporated in Eq. (4) and ABP with arbitrary activity can be accomplished with this simple modeling. In this sense, the dumbbell model can be regarded as an ABP model implemented in this work with a certain D_r value.

(iii) Once D_r is used as an input parameter, the relation between D_r and τ_r can be quantified directly after τ_r is acquired by fitting the orientational time correlation function.

(iv) Note that however, this modified ABP model is not applicable of the investigation of hydrodynamic behaviors. When the suspension is non-dilute and hydrodynamic interactions play a role, this model is no longer viable and the dumbbell model needs to be employed.

2.2.2. Orientational persistence time

For an ABP whose orientation is governed by Eq. (4), it can be numerically verified that the orientational time correlation function $C(t)$ can be expressed by an exponential function

$$C(t) = \langle \boldsymbol{n}(t) \cdot \boldsymbol{n}(0) \rangle = \mathrm{e}^{-t/\tau_r}, \tag{5}$$

where τ_r is the orientational persistence time. For spherical particles in three-dimensional space, the orientational persistence time τ_r is directly related to the rotational diffusivity D_r through the relation[3]

$$\tau_r = \frac{1}{2D_r}. \tag{6}$$

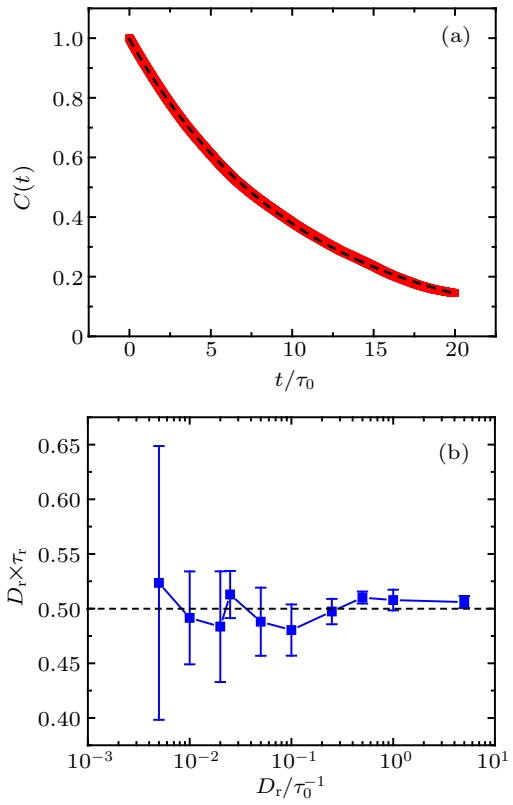


Fig. 2. (a) Exponential decay of the orientational time correlation function $C(t)$ for $D_r = 0.05\tau_0^{-1}$. The red solid line represents the numerical result and the black dashed line represents the exponential fitting with $\tau_r = 10.32\tau_0$. (b) The product $D_r \times \tau_r$ plotted for different values of D_r in units of τ_0^{-1}. Note that for small D_r, τ_r is large and leads to large statistical error in a limited time duration.

In Fig. 2(a), an ABP with $D_r = 0.05\tau_0^{-1}$ is taken as an example to show $C(t)$ as a function of time. It is readily seen that the numerical result for $C(t)$ can be fitted by Eq. (5) with $\tau_r = 10.32\tau_0$, which is related to D_r via Eq. (6) within statistical error.

In Fig. 2(b), the product of D_r and τ_r is plotted for different values of D_r. It is seen that the numerical value fluctuates around the theoretical value 1/2. For each value of D_r, $C(t)$ is calculated for five times to obtain the error bar. It is noted that for $D_r < 0.005\tau_0^{-1}$, we have $\tau_r > 100\tau_0$. Limited by the sampling time for obtaining $C(t)$, we have large statistical error for long persistence time.

Finally, we would like to point out that in our MD simulations, the particle orientation is directly taken from $\boldsymbol{n}$ which is obtained by solving Eq. (4). Therefore, although the active particle is surrounded by fluid particles, its orientation is not affected by the collisions with fluid particles, and the orientational time correlation function is solely controlled by the parameter D_r. In our MD simulations, the force dipole is exerted on the ABP in the direction of $\boldsymbol{n}$, along which the active velocity is acquired and to be measured. Note that in the presence of thermal noises, the instantaneous velocity of the active particle is by no means in the direction of $\boldsymbol{n}$, making a trajectory that is strongly fluctuating in time.

2.2.3. Active velocity

Besides the orientational persistence time, the active velocity in the direction of particle orientation is another key characteristic that controls the ABP dynamics. In the commonly used minimal model described by Eqs. (3) and (4), the active velocity in the direction of $\boldsymbol{n}$ has a constant magnitude. However, this is no longer the case in our MD simulations. For an active particle driven by the force dipole applied in the direction of $\boldsymbol{n}$, the axial velocity $w_A \equiv \dot{\boldsymbol{r}} \cdot \boldsymbol{n}$ is measured at each time step in the same direction. Due to the frequent collisions with surrounding fluid particles, the axial velocity exhibits a Gaussian distribution, as shown in Fig. 3(a). Some interesting observations on the axial velocity are summarized as follows:

(i) The axial velocity w_A exhibits standard Gaussian distribution. Its mean and variance are called the active velocity v_A and axial velocity variance σ_A^2, respectively.

(ii) Once the size of the active particle is fixed, the active velocity v_A increases with the increasing force F_A linearly, as shown in Fig. 3(b). Furthermore, v_A is found to be independent of D_r or τ_r. We will take the mean v_A as the active velocity in the Langevin Eq. (3).

(iii) The magnitude of v_A measured in MD simulations is consistent with the hydrodynamic estimation. Mathematically, the flow induced at position $\boldsymbol{r}$ measured from the force dipole $\boldsymbol{p} = p\boldsymbol{n}$ is given by[3,20]

$$\boldsymbol{u}(\boldsymbol{r}) = \frac{p}{8\pi\eta r^3}\left[3\cos^2\theta - 1\right]\boldsymbol{r}, \tag{7}$$

in which η is the shear viscosity and θ is the angle between $\boldsymbol{r}$ and $\boldsymbol{n}$. Figure 3(b) shows that the ratio of v_A to

F_A is $\sim 0.01\tau_0 m_f^{-1}$, which quantitatively agrees with $v_A = F_A \times 5\sigma_{ff} \times 2/8\pi\eta l^2$ for $\theta = 0$, in which $5\sigma_{ff}$ is the distance between the center of the head particle and the center of the fluid phantom region (see Fig. 1(b)), $\eta = 2.5 m_f \sigma_{ff}^{-1} \tau_0^{-1}$ is used for the viscosity, and $l = 4\sigma_{ff}$ is used for the typical length scale. This agreement suggests that the ABP swims in the surrounding liquid as a pusher. Regarding the temperature control in our MD simulations, we would like to point out that the Langevin thermostat applied to each solvent particle does not preserve the momentum conservation locally. In fact, the effect of the thermostat in non-equilibrium MD simulations has been investigated for decades.[47] Although our simulations are expected to be capable of semi-quantitatively reproducing the near field of a pusher, as seen from the magnitude of v_A, we are not sure if the far flow field as described by Eq. (7) can be reproduced. The small magnitude of the far field also makes it very difficult to measure accurately.

(iv) Once the size of the active particle is fixed, σ_A^2 is independent of F_A.

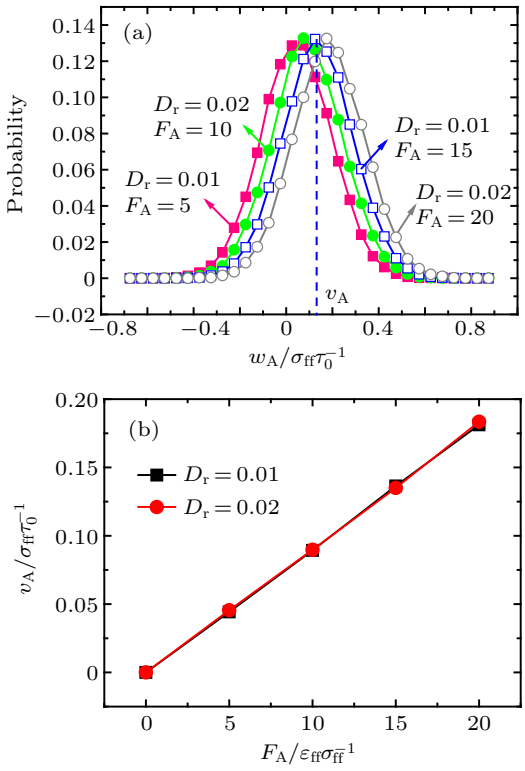


Fig. 3. (a) Gaussian distribution of the axial velocity w_A, plotted for different values of rotational diffusivity D_r (in units of τ_0^{-1}) and applied force F_A (in units of $\varepsilon_{ff}\sigma_{ff}^{-1}$). (b) The active velocity v_A plotted as a function of the applied force F_A for $D_r = 0.01\tau_0^{-1}$ and $0.02\tau_0^{-1}$.

Based on the above observations, it can be concluded that the active velocity is instantaneously induced by the applied force dipole (given by $F_A \times 5\sigma_{ff}$ here), with its magnitude predicted by Eq. (7) semi-quantitatively. Furthermore, the active particle is subject to the random force dipole originating from the collisions with fluid particles, and hence shows a variance in the distribution of axial velocity.

For swimming organisms such as cells and bacteria, the size of a swimmer is typically larger than that of the fluid particle by several orders of magnitude. As a result, the ratio of the standard deviation σ_A to the active velocity v_A is negligible. In our MD simulations, however, the active particle is not that big compared to the fluid particles (see Fig. 1(b)), and hence the standard deviation σ_A becomes appreciably large. It is interesting to observe how σ_A would scale with the size of ABP. For this purpose, a length parameter L is introduced to measure the size of ABP, with $L = 1$ corresponding to the ABP illustrated in Fig. 1(b). Note that when L is increased, all the length parameters are increased in proportion, including the length scale in the WCA potential for head particles, the radius of the fluid phantom region, and the distance between the head particle and the fluid phantom region. Figure 4 shows that the standard deviation σ_A does decrease with the increasing L. A theoretical argument can be made to predict $\sigma_A \propto L^{-1/2}$, which is indeed indicated by Fig. 4.

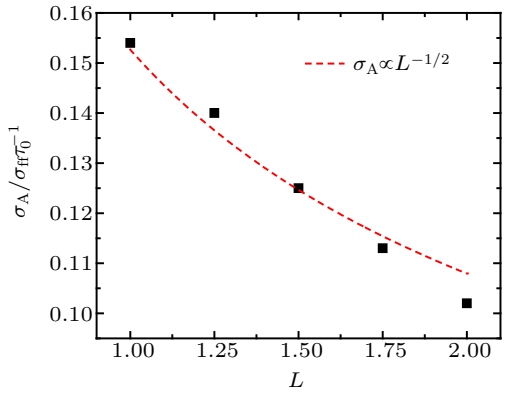


Fig. 4. Dependence of the standard deviation σ_A on the size of ABP.

2.2.4. Critical persistence length

In the present work, the particle orientation $\boldsymbol{n}$ evolves according to Eq. (4) and is supplied to the MD simulations as external input. Theoretically, any orientational persistence time τ_r can be used. However, if τ_r is very short, then the effect of the active velocity $v_A\boldsymbol{n}$ in Eq. (3) becomes that of the white noises with no time correlation. In our MD simulations, we find that to make the active particles behave truly 'actively', the persistence time τ_r has to be sufficiently large. While we understand that this is only from a phenomenological perspective, we believe that a sufficiently large τ_r is necessary for the ABPs to behave differently from PBPs. This will be made evident in the next two sections.

Figure 5 shows the trajectories for different values of the persistence length l_A defined by

$$l_A = v_A \tau_r, \tag{8}$$

which quantifies the step length for an active particle's random walk. It is seen that the trajectory of the ABP of $l_A = 0.18\sigma_{ff}$ exhibits a random walk of very short step length, which is very much close to that of a PBP. In this case the persistence

time $\tau_r = 1\tau_0$ is very short. Although a large active velocity $v_A = 0.18\sigma_{ff}\tau_0^{-1}$ is used, the persistence length $l_A = 0.18\sigma_{ff}$ is still very short and the active particle shows no appreciable difference from a PBP. As the persistence length is increased to $l_A = 4.5\sigma_{ff}$, the trajectory is formed by a sequence of 'straight' lines. In this case the ABP behaves truly actively, capable of exploring a much larger space compared to that of the PBP.

Through our simulations, we find that the self-propelled motion of ABP can be effectively distinguished from the random walk of PBP if the persistence length exceeds $l_A = 1.125\sigma_{ff}$, as illustrated in Fig. 5. The critical persistence length is therefore taken at $\sim 1\sigma_{ff}$. In the results presented below, $l_A = 1.125\sigma_{ff}$ serves as the lower bound for all the active particles.

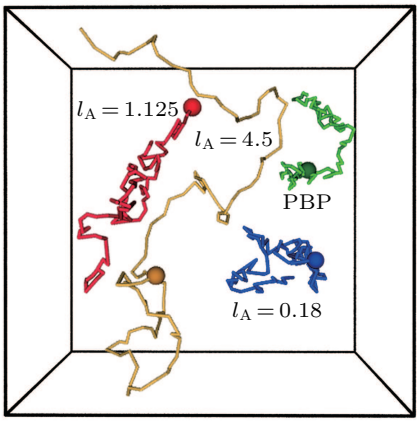


Fig. 5. Trajectories of a PBP and three ABPs with $l_A = 0.18\sigma_{ff}$ from $\tau_r = 1\tau_0, v_A = 0.18\sigma_{ff}\tau_0^{-1}$, $l_A = 1.125\sigma_{ff}$ from $\tau_r = 25\tau_0, v_A = 0.045\sigma_{ff}\tau_0^{-1}$, and $l_A = 4.5\sigma_{ff}$ from $\tau_r = 50\tau_0$, $v_A = 0.09\sigma_{ff}\tau_0^{-1}$. Each trajectory includes 100 frames with a time duration of $25\tau_0$.

3. Active Brownian particles in free space

Both PBPs and ABPs exhibit ballistic motion at short time scales, but enter into the regime of diffusive motion at long time scales.[25] Here we measure the effective diffusivity for ABPs in free space without confining potential.

We start from the diffusivity of a PBP for reference. The PBP used for this purpose is just the head particle. No phantom region of fluid is introduced and no external force dipole is applied either. To reduce the statistical fluctuations, simulations have been performed for many times with different initial conditions. From the mean square displacement (MSD) which increases with time linearly as shown in Fig. 6(a), we obtain the translational diffusion coefficient D_T from

$$D_T = \frac{\left\langle |\boldsymbol{r}(t) - \boldsymbol{r}(0)|^2 \right\rangle_{PBP}}{6t}. \tag{9}$$

Through a linear fitting, D_T is found to be $0.015\sigma_{ff}^2\tau_0^{-1}$. According to the Einstein relation $\gamma D_T = k_B T$, the drag coefficient γ is approximately $100 m_f \tau_0^{-1}$. Using the Stokes drag coefficient $\gamma = 6\pi\eta R$ for a spherical particle and $\eta = 2.5 m_f \sigma_{ff}^{-1}\tau_0^{-1}$ for the viscosity, it is estimated that the radius of the PBP is about $2\sigma_{ff}$. This is consistent with the fact that the interaction between head and fluid particles is modeled by a LJ potential with length scale $\sigma_{af} = (\sigma_{aa} + \sigma_{ff})/2 = 2\sigma_{ff}$.

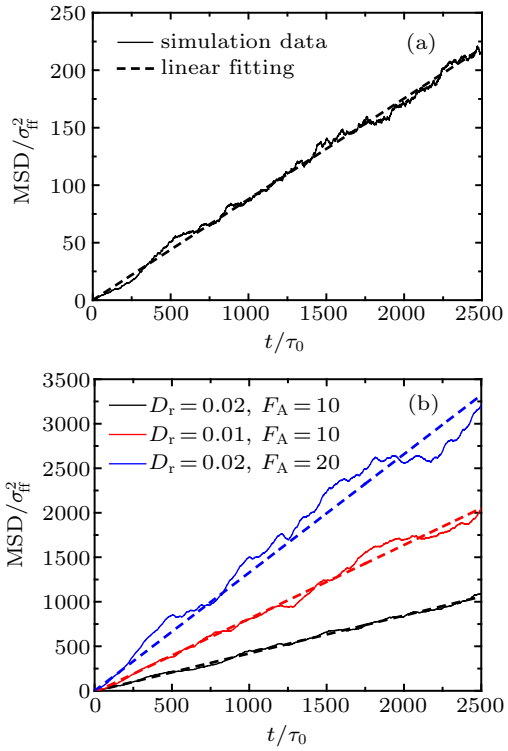


Fig. 6. (a) MSD for PBPs (solid line), with D_T found to be $0.015\sigma_{ff}^2\tau_0^{-1}$ through a linear fitting (dashed line). (b) MSD for three ABPs with different values of D_r (in units of τ_0^{-1}) and F_A (in units of $\varepsilon_{ff}\sigma_{ff}^{-1}$). In each case, the solid line represents the simulation data and the dashed line of the same color represents the corresponding linear fitting.

Now we turn to ABPs with $D_r = 0.01\tau_0^{-1}$ and $0.02\tau_0^{-1}$ subject to several different values of the active force F_A. To reduce the statistical fluctuations, simulations have been performed for many times with different initial conditions and different orientational trajectories of $\boldsymbol{n}$. Figure 6(b) shows the MSD results for three representative ABPs in a time duration of $2500\tau_0$. Although the MSD lines do exhibit a linear increase with time, it is noted that statistical fluctuations are amplified by the increase of the effective diffusivity itself. This is due to the insufficiency of sampling in the limited time duration. Compared with the PBP result in Fig. 6(a), figure 6(b) shows that the diffusive motion of ABPs is much faster, with a much larger effective diffusion coefficient D_E defined by

$$D_E = \frac{\left\langle |\boldsymbol{r}(t) - \boldsymbol{r}(0)|^2 \right\rangle_{ABP}}{6t}. \tag{10}$$

Subtracting the passive part D_T from D_E, we obtain the active diffusion coefficient $D_A \equiv D_E - D_T$, which measures the contribution of self-propelled motion to diffusion. For the ABPs modeled by Eqs. (3) and (4), D_A is given by[3]

$$D_A = \frac{v_A^2 \tau_r}{3}. \tag{11}$$

While equations (3) and (4) only describe the ABPs in a minimal model, it is still interesting to see if the MD results obtained here support $D_{\rm A} \propto v_{\rm A}^2 \tau_{\rm r}$.

Figure 7 shows the dependence of $D_{\rm A}$ on $v_{\rm A}^2$ for two different values of $D_{\rm r}$. It is seen that for a given $D_{\rm r}$, $D_{\rm A}$ increases with $v_{\rm A}^2$ linearly. Furthermore, the slope for $D_{\rm r} = 0.01\tau_0^{-1}$ is approximately twice as big as that for $D_{\rm r} = 0.02\tau_0^{-1}$, indicating $D_{\rm A} \propto v_{\rm A}^2 \tau_{\rm r}$ with $\tau_{\rm r} = 1/2D_{\rm r}$. Although our MD simulation results support $D_{\rm A} \propto v_{\rm A}^2 \tau_{\rm r}$, the prefactor α in $D_{\rm A} \simeq \alpha v_{\rm A}^2 \tau_{\rm r}$ is found to be less than $1/3$ predicted by the minimal model in Eq. (11). This may be attributed to the additional complexities which are inherent in our MD simulations and beyond the description by Eqs. (3) and (4). These include:

(i) Due to the frequent collisions of the active particle with surrounding fluid particles, the axial velocity $w_{\rm A}$ exhibits a Gaussian distribution, with the active velocity $v_{\rm A}$ defined as the mean of $w_{\rm A}$ (see Fig. 3). The use of a constant $v_{\rm A}$ in Eq. (3) is an oversimplification.

(ii) The orientational persistence time $\tau_{\rm r}$ is associated with the time evolution of particle orientation $\boldsymbol{n}$. Although the force dipole is applied in the direction of $\boldsymbol{n}$, the induced velocity may deviate from this direction due to various noises in MD simulations. The use of $v_{\rm A}\boldsymbol{n}$ in Eq. (3) is an oversimplification again.

(iii) According to the way the ABP is constructed (see Fig. 1(b)), the active particle is by no means spherical and the use of $D_{\rm T}$ for a spherical particle in Eq. (3) is an oversimplification yet again.

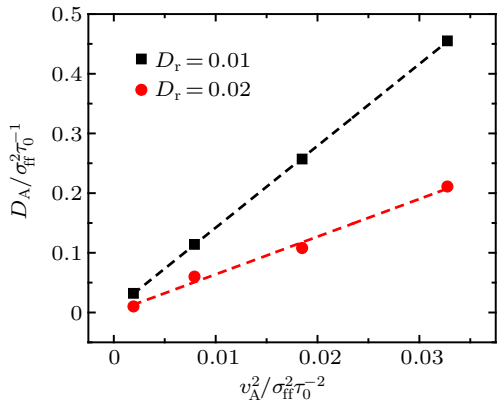


Fig. 7. MD simulation results for the dependence of $D_{\rm A}$ on $v_{\rm A}^2$ for $D_{\rm r} = 0.01\tau_0^{-1}$ and $0.02\tau_0^{-1}$. From the linear fitting (dashed lines), the prefactor α in $D_{\rm A} \simeq \alpha v_{\rm A}^2 \tau_{\rm r}$ is found to be 0.274 for $D_{\rm r} = 0.01\tau_0^{-1}$ and 0.252 for $D_{\rm r} = 0.02\tau_0^{-1}$.

4. Active Brownian particles in confinement

In this section we investigate the distribution of non-interacting ABPs confined by an isotropic harmonic potential $U(r) = kr^2/2$, with the distance r measured from the center of the simulation box. A series of different values for the spring constant k (in units of $\varepsilon_{\rm ff}\sigma_{\rm ff}^{-2}$) will be used to explore different regimes of confinement. Time averaging is performed over an ensemble of particle trajectories. For weaker confinement, longer time averaging is needed to remove statistical fluctuations.

4.1. Boltzmann distribution of passive Brownian particles

We start from the Boltzmann distribution of a PBP. The PBP used for this purpose is still the head particle, with no phantom region and no external force dipole. The equilibrium probability density function (PDF) $g(r)$ is given by the Boltzmann distribution

$$g(r) \propto {\rm e}^{-\frac{kr^2}{2k_{\rm B}T}}. \tag{12}$$

Figure 8 shows $g(r)$ as a function of r for the spring constant $k = \varepsilon_{\rm ff}\sigma_{\rm ff}^{-2}$. Note that the PDF $g(r)$ is defined for $r \geqslant 0$ with the normalization condition

$$\int_0^\infty g(r) 4\pi r^2 {\rm d}r = 1. \tag{13}$$

To better present $g(r)$ visually, r is extended to cover $(-\infty, +\infty)$ and the data for $r \geqslant 0$ are mirrored to the negative half of r axis, with the curve of $g(r)$ being symmetric about $r = 0$. This applies to all the $g(r)$ curves in this section. Figure 8 shows that the numerical result for $g(r)$ is quantitatively described by Eq. (12). Such agreement is also achieved for other values of the spring constant.

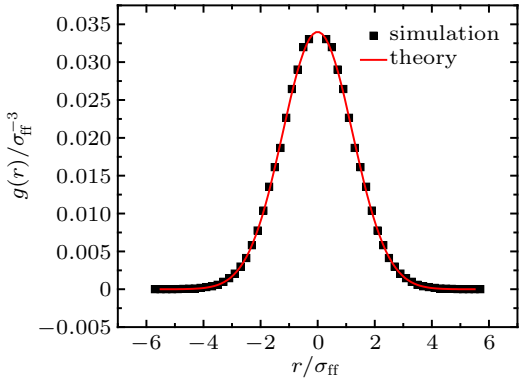


Fig. 8. The equilibrium PDF $g(r)$ of the confined PBP for $k = \varepsilon_{\rm ff}\sigma_{\rm ff}^{-2}$.

4.2. Stationary distribution of active Brownian particles

Now we consider an ABP confined by the harmonic potential $U(r) = kr^2/2$ and focus on its stationary PDF $g(r)$. To understand the physical picture, we start from a minimal model described by Eq. (4) and

$$\dot{\boldsymbol{r}} = -\mu\nabla U + v_{\rm A}\boldsymbol{n} + \sqrt{2D_{\rm T}}\boldsymbol{\xi}, \tag{14}$$

in which μ is the mobility coefficient, which is the inverse of the drag coefficient γ. Compared with Eq. (3), equation (14) includes an additional term $-\mu\nabla U$ due to the confining potential U. In the limit of $D_{\rm T} \to 0$, the particle motion is confined by the boundary $r = r_{\rm B}$ with $r_{\rm B}$ given by

$$r_{\rm B} = \frac{v_{\rm A}}{\mu k}. \tag{15}$$

At finite D_T, the particle can still go beyond $r = r_B$ with the assistance of thermal noises. The relaxation time for the over-damped motion in the confining potential U is $1/\mu k$, and the other time scale is the orientational persistence time τ_r. Here we introduce a dimensionless parameter R_1 to measure the ratio of τ_r to $1/\mu k$,

$$R_1 = \frac{\tau_r}{1/\mu k} = \mu k \tau_r. \tag{16}$$

When $R_1 \ll 1$, the orientational persistence time τ_r is very short compared to $1/\mu k$, and the active term $v_A \boldsymbol{n}$ plays the role of white noises effectively. This leads to a Boltzmann-type distribution of ABP given by $g_B(r) \propto \exp\left(-\mu k r^2/2D_E\right)$, with the effective temperature given by $k_B T_E = D_E/\mu$ where D_E is the effective diffusivity. The width of this distribution is about $\sqrt{D_E/\mu k}$. Another dimensionless parameter R_2 can be introduced to measure the ratio of $\sqrt{D_E/\mu k}$ to r_B. Using $D_E = D_T + D_A \approx D_A$ and $D_A \approx \alpha v_A^2 \tau_r$, we have

$$R_2 \approx \sqrt{\frac{v_A^2 \tau_r}{\mu k}} \Big/ \frac{v_A}{\mu k} = \sqrt{\mu k \tau_r}, \tag{17}$$

which is $\sqrt{R_1}$. It follows that when $R_1 \ll 1$, $R_2 \ll 1$ as well. This means that the Boltzmann-type distribution $g_B(r)$ can be realized and accommodated within the boundary $r = r_B$.

The fact that $R_1 \ll 1$ leads to $R_2 \ll 1$ can be regarded as a self-consistency check. From $R_1 \ll 1$, the particle activity can be effectively taken as white noises with $\tau_r \to 0$. As a result, the Boltzmann-type distribution is expected to occur at the effective temperature T_E. This distribution is then found to be much narrower than the boundary set by the confinement potential and the particle activity, and hence it is realizable.

The self-consistency check above also indicates that the Boltzmann-type distribution $g_B(r)$ will be invalidated by the increase of R_1. For $R_1 \sim 1$, this distribution would meet the confinement boundary $r = r_B$ and hence can no longer be realized. In fact, when τ_r becomes comparable to $1/\mu k$, the PDF $g(r)$ shows a plateau rather than a peak around $r = 0$. When τ_r becomes much larger than $1/\mu k$, the ABP spends a short time ($\sim 1/\mu k$) traveling in the potential field but a long time ($\sim \tau_r$) staying near the boundary $r = r_B$ before turning around. This corresponds to the accumulation of probability at the confinement boundary, with the PDF $g(r)$ showing a bimodal distribution peaked near $r = \pm r_B$. The larger R_1 is, the sharper the peak is.

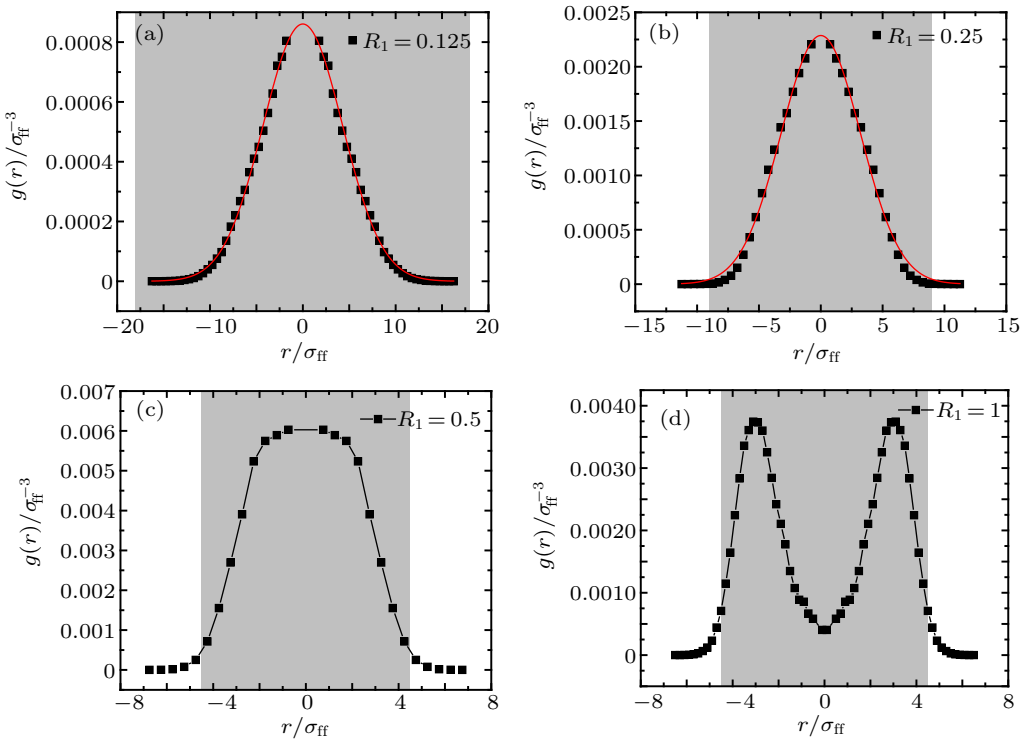


Fig. 9. Evolution of the PDF $g(r)$ with the increase of R_1. (a) The Boltzmann-type distribution for $R_1 = 0.125$. (b) A distribution slightly deviating from the Boltzmann-type for $R_1 = 0.25$. (c) A distribution exhibiting a plateau in the central region for $R_1 = 0.5$. (d) A bimodal distribution for $R_1 = 1$ with the accumulation of probability near $r = \pm r_B$. Here the red line represents a fitting of the Boltzmann-type and the gray region is bounded by $r = \pm r_B$.

In consistency with the above discussion, our MD simulations have shown how the stationary PDF $g(r)$ evolves with the change of R_1. The same $\tau_r = 25\tau_0$ is used for all the four cases presented below. Figures 9(a)–9(c) are produced for an ABP with $v_A = 0.09\sigma_{ff}\tau_0^{-1}$ using different values of k. Limited by the computational capability, it is unrealistic to have a confinement potential with a very small value of k and hence a very wide distribution. Figure 9(a) shows the case for $k = 0.5\varepsilon_{ff}\sigma_{ff}^{-2}$, from which we have $R_1 = 0.125$ and $r_B = 18\sigma_{ff}$ using the drag coefficient $\gamma = 100 m_f \tau_0^{-1}$ and

$\mu = 1/\gamma$. This is the smallest value of R_1 we can access. The Boltzmann-type distribution is well maintained at this value of R_1. Here the red line represents a fitting of the Boltzmann-type and the gray region is bounded by $r = \pm r_B$. In this case, the particle distribution is completely within the confinement boundary. Figure 9(b) shows the case for $k = \varepsilon_{ff}\sigma_{ff}^{-2}$, $R_1 = 0.25$, and $r_B = 9\sigma_{ff}$. In this case, the particle distribution touches the confinement boundary and hence slightly deviates from the Boltzmann-type distribution. Figure 9(c) shows the case for $k = 2\varepsilon_{ff}\sigma_{ff}^{-2}$, $R_1 = 0.5$, and $r_B = 4.5\sigma_{ff}$. In this case, the particle distribution is appreciably different from the Boltzmann-type and exhibits a plateau in the central region. Finally, figure 9(d) shows the case for $k = 4\varepsilon_{ff}\sigma_{ff}^{-2}$, $R_1 = 1$, and $r_B = 4.5\sigma_{ff}$. Here a larger active velocity $v_A = 0.18\sigma_{ff}\tau_0^{-1}$ is used to ensure that r_B is not too small. This is to avoid the domination of thermal noises in a very narrow region. In this case, the particle distribution is bimodal, corresponding to the accumulation of probability near $r = \pm r_B$.

4.3. A quantitative analysis for the stationary distribution

In order to measure the active diffusion coefficient in confinement potential, a quantitative analysis is carried out by focusing on the stochastic dynamics of the x coordinate. The x component of Eq. (14) can be written as

$$\dot{x}(t) = -\mu k x(t) + \sqrt{2D_A}\phi(t) + \sqrt{2D_T}\xi_x, \tag{18}$$

where ϕ is a colored noise due to the active motion and ξ_x is the zero-mean unit-variance Gaussian white noise in the x direction, with

$$\langle \phi(t_2)\phi(t_1)\rangle = \frac{1}{2\tau_r} e^{-|t_2-t_1|/\tau_r}, \tag{19}$$

$$\langle \xi_x(t_2)\xi_x(t_1)\rangle = \delta(t_2 - t_1). \tag{20}$$

At sufficiently large t, the mean square displacement of x with respect to $r = 0$ can be analytically expressed as

$$\langle x^2\rangle = \frac{D_A}{\mu k(\mu k\tau_r + 1)} + \frac{D_T}{\mu k}, \tag{21}$$

in which the contribution of the colored noise shows a dependence on $R_1 = \mu k\tau_r$. In the limit of $R_1 \to 0$, ϕ is effectively a white noise and we have $\langle x^2\rangle = (D_A + D_T)/\mu k = D_E/\mu k$, which is in agreement with the Boltzmann-type distribution $g_B(r) \propto \exp(-\mu k r^2/2D_E)$ discussed above. However, when τ_r becomes comparable to $1/\mu k$, the correction by $1/(\mu k\tau_r + 1)$ needs to be taken into consideration.

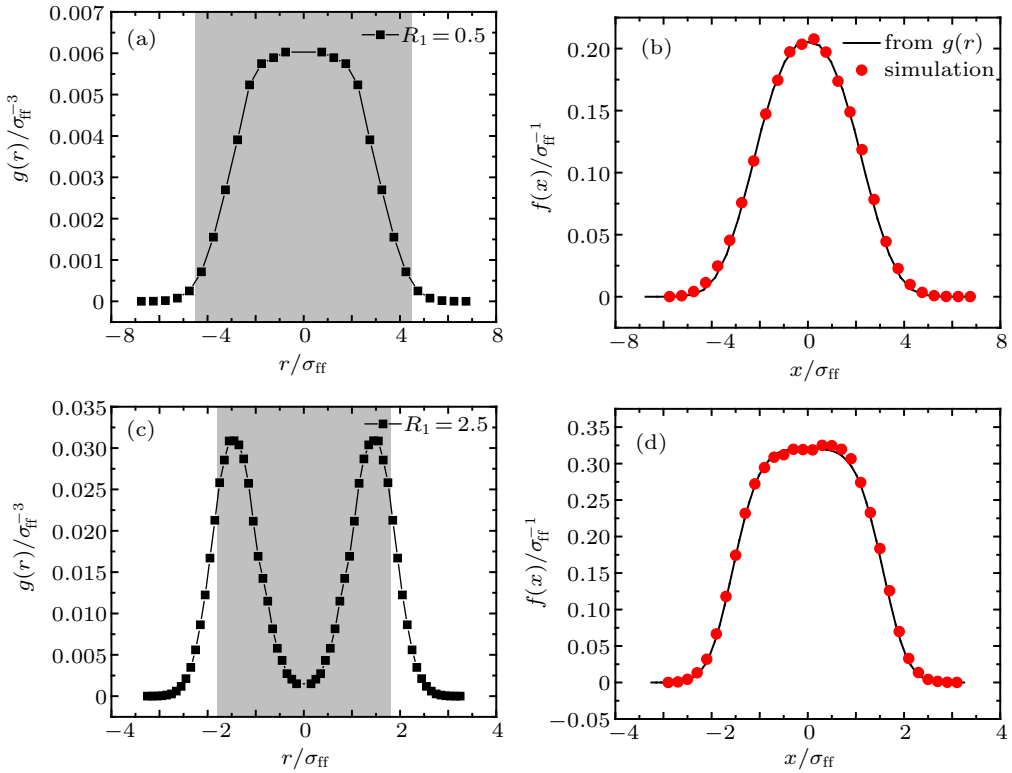


Fig. 10. The PDF $g(r)$ and marginal PDF $f(x)$. (a) $g(r)$ for $R_1 = 0.5$. (b) $f(x)$ for $R_1 = 0.5$. (c) $g(r)$ for $R_1 = 2.5$. (d) $f(x)$ for $R_1 = 2.5$. In (b) and (d), $f(x)$ directly measured in simulations (represented by solid circles) is compared to that obtained from $g(r)$ by the use of Eq. (23) (represented by solid line), with good agreement.

In our MD simulations, $\langle x^2\rangle$ is computed according to its definition

$$\langle x^2\rangle = \int_0^\infty x^2 f(x)\,dx, \tag{22}$$

where $f(x)$ is the stationary marginal PDF of the x coordinate, which can be measured directly. It can also be obtained by measuring the stationary PDF $g(r)$ and performing the inte-

gration as

$$f(x) = \int_{-\infty}^{\infty}\int_{-\infty}^{\infty} g\left(\sqrt{x^2+y^2+z^2}\right)\mathrm{d}y\mathrm{d}z = \int_{0}^{\infty} g\left(\sqrt{x^2+\rho^2}\right)2\pi\rho\mathrm{d}\rho. \quad (23)$$

Figure 10 shows the marginal PDF for $R_1 = 0.5$ and 2.5. The two sets of data are in good agreement, one directly measured in simulations, and the other obtained from $g(r)$ by the use of Eq. (23).

We can easily compute $\langle x^2 \rangle$ by measuring $f(x)$ and using Eq. (22). We then substitute the value of $\langle x^2 \rangle$ into Eq. (21) to deduce the value of D_A. This involves the use of $D_\mathrm{T} = 0.015\sigma_\mathrm{ff}^2\tau_0^{-1}$ measured in Section 3, $\mu = 1/\gamma$ with $\gamma = 100m_\mathrm{f}\tau_0^{-1}$ such that $\gamma D_\mathrm{T} = k_\mathrm{B}T = 1.5\varepsilon_\mathrm{ff}$, and $\tau_\mathrm{r} = 1/2D_\mathrm{r} = 25\tau_0$ with $D_\mathrm{r} = 0.02\tau_0^{-1}$ used in Eq. (4) for the orientational dynamics. The value of D_A so deduced from $\langle x^2 \rangle$ in the confinement potential is denoted by D_AC here. On the other hand, the active part of the diffusion coefficient $D_\mathrm{A} \equiv D_\mathrm{E} - D_\mathrm{T}$, obtained by measuring D_E in free space (presented in section 3), is denoted by D_AF here. A comparison between D_AC and D_AF is made in Table 1 for six different values of R_1 from 0.125 ($\ll 1$) to 10 ($\gg 1$). It is readily seen that D_AF is always less than D_AC by about 15% to 29%. It is also interesting to note that the values of D_AC show a better agreement with the relation $D_\mathrm{A} \propto v_\mathrm{A}^2$, with $0.29/0.07 \approx (0.18/0.09)^2$.

Table 1. Comparison between D_AC and D_AF.

R_1	$v_\mathrm{A}/(\sigma_\mathrm{ff}\tau_0^{-1})$	$\langle x^2 \rangle/\sigma_\mathrm{ff}^2$	$D_\mathrm{AC}/(\sigma_\mathrm{ff}^2/\tau_0)$	$D_\mathrm{AF}/(\sigma_\mathrm{ff}^2/\tau_0)$	Error/%
0.125	0.09	15.77	0.072	0.058	19.4
0.25	0.09	7.29	0.072	0.058	19.4
0.5	0.09	3.05	0.069	0.058	15.9
1	0.18	3.98	0.288	0.208	27.7
2.5	0.18	0.98	0.291	0.208	28.5
10	0.18	0.10	0.275	0.208	24.4

Finally, to comment on this comparison and the relation $D_\mathrm{A} \propto v_\mathrm{A}^2$ being better satisfied by D_AC, we would like to point out the following:

(i) As discussed at the end of Section 3, the ABPs in our MD simulations involve additional complexities that are beyond the description by Eqs. (3), (4), and (14), from which $D_\mathrm{AC} = D_\mathrm{AF}$ is expected.

(ii) The relative difference between D_AC and D_AF is always smaller than 29%. This means that the minimal model based on Eqs. (3), (4), and (14) is semi-quantitatively accurate to describe the ABPs, for R_1 varying over two orders of magnitude (from 0.125 to 10).

(iii) In the confinement potential, the particle trajectories show better statistical convergence than in free space. This could be the reason for $D_\mathrm{A} \propto v_\mathrm{A}^2$ being better satisfied by D_AC.

5. Conclusions

ABP model consisting of a solid body and a forced fluid body has been implemented in MD simulations. Each active particle consists of a head particle and a spherical phantom region of fluid where the flagellum takes effect. The stochastic dynamics of particle orientation is controlled by the rotational Gaussian white noises, and the orientational persistence time τ_r is solely determined by the rotational diffusivity D_r through the relation $\tau_\mathrm{r} = 1/2D_\mathrm{r}$. Due to the frequent collisions of the active particle with surrounding fluid particles, the axial velocity w_A of the active particle exhibits a Gaussian distribution. The mean value of w_A is defined as the active velocity v_A, which increases with the active force F_A linearly but shows no dependence on D_r.

For the active diffusion coefficients measured in free space and in confinement with this newly implemented ABP model, our MD simulations show the following results. (i) The active diffusion coefficient D_A measured in free space supports the relation $D_\mathrm{A} \propto v_\mathrm{A}^2\tau_\mathrm{r}$ although the proportionality constant deviates from $1/3$ predicted by the minimal model. (ii) From the stationary particle distribution in the confinement potential, the active diffusion coefficient is measured and then compared to that measured in free space, with the relative difference always less than 29%. (iii) This semi-quantitative agreement is fairly good because the comparison has been carried out for $\mu k\tau_\mathrm{r}$ varying over two orders of magnitude.

These results demonstrate that the modeling realized in our MD simulations is able to capture the salient features of the overdamped ABPs described by the minimal model. The common and convenient use of the minimal model is therefore justified on the one hand. On the other hand, the validity of the dumbbell model as an ABP is also confirmed in our MD simulations, which consider the effects of both momentum transport and thermal fluctuations in the surrounding liquids. We understand that the simulation method is yet to be improved in applying the thermostat[47] (with the consideration of local momentum conservation) and computational efficiency (in comparison with, e.g., dissipative particle dynamics[48]). As the dumbbell-modeled active particles can interact with each other via hydrodynamic coupling, many interesting collective phenomena may emerge in a fluctuating environment. This represents a direction to be pursued that requires further improvement of the simulation method.

References

[1] Ramaswamy S 2010 *Annu. Rev. Condens. Matter Phys.* **1** 323
[2] Bechinger C, Di Leonardo R, Löwen H, Reichhardt C, Volpe G and Volpe G 2016 *Rev. Mod. Phys.* **88** 045006
[3] Zöttl A and Stark H 2016 *J. Phys.: Condens. Matter* **28** 253001
[4] Romanczuk P, Bär M, Ebeling W, Lindner B and Schimansky-Geier L 2012 *Eur. Phys. J. Spec. Top.* **202** 1
[5] Berg H C and Anderson R A 1973 *Nature* **245** 380

[6] Cisneros L H, Kessler J O, Ganguly S and Goldstein R E 2011 *Phys. Rev. E* **83** 061907
[7] Cates M E 2012 *Rep. Prog. Phys.* **75** 042601
[8] Harshey R M 2003 *Annu. Rev. Microbiol.* **57** 249
[9] Selmeczi D, Li L, Pedersen L I, Nrrelykke S, Hagedorn P H, Mosler S, Larsen N B, Cox E C and Flyvbjerg H 2008 *Eur. Phys. J. Spec. Top.* **157** 1
[10] Boedeker H U, Beta C, Frank T D and Bodenschatz E 2010 *Europhys. Lett.* **90** 28005
[11] Friedrich B M and Jülicher F 2007 *Proc. Natl. Acad. Sci. USA* **104** 13256
[12] Buttinoni I, Bialké J, Kümmel F, Löwen H, Bechinger C and Speck T 2013 *Phys. Rev. Lett.* **110** 238301
[13] Palacci J, Cottin-Bizonne C, Ybert C and Bocquet L 2010 *Phys. Rev. Lett.* **105** 088304
[14] Volpe G, Gigan S and Volpe G 2014 *Am. J. Phys.* **82** 659
[15] Marchetti M C, Joanny J F , Ramaswamy S, Liverpool T B, Prost J, Rao M and Simha R A 2013 *Rev. Mod. Phys.* **85** 1143
[16] Purcell E M 1977 *Am. J. Phys.* **45** 3
[17] Chen X, Yang X, Yang M and Zhang H 2015 *EPL* **111** 54002
[18] Lauga E 2016 *Annu. Rev. Fluid Mech.* **48** 105
[19] Furukawa A, Marenduzzo D and Cates M E 2014 *Phys. Rev. E* **90** 022303
[20] Lauga E and Powers T R 2009 *Rep. Prog. Phys.* **72** 096601
[21] Hernandez-Ortiz J P, Stoltz C G and Graham M D 2005 *Phys. Rev. Lett.* **95** 204501
[22] Elgeti J, Winkler R and Gompper G 2015 *Rep. Prog. Phys.* **78** 056601
[23] Baskaran A and Marchetti M C 2009 *Proc. Natl. Acad. Sci. USA* **106** 15567
[24] de Graaf J, Menke H, Mathijssen A J, Fabritius M, Holm C and Shendruk T N 2016 *J. Chem. Phys.* **144** 134106
[25] Howse J R, Jones R A, Ryan A J, Gough T, Vafabakhsh R and Golestanian R 2007 *Phys. Rev. Lett.* **99** 048102
[26] Ai B Q and Li F G 2017 *Soft Matter* **13** 2536
[27] Suma A, Gonnella G, Marenduzzo D and Orlandini E 2014 *Europhys. Lett.* **108** 56004
[28] Peruani F, Deutsch A and Bär M 2006 *Phys. Rev. E* **74** 030904
[29] Kudrolli A, Lumay G, Volfson D and Tsimring L S 2008 *Phys. Rev. Lett.* **100** 058001
[30] Gao T and Li Z 2017 *Phys. Rev. Lett.* **119** 108002
[31] Cates M and Tailleur J 2013 *EPL* **101** 20010
[32] Menzel A M 2015 *Phy. Rep.* **554** 1
[33] Stenhammar J, Tiribocchi A, Allen R J, Marenduzzo D and Cates M E 2013 *Phys. Rev. Lett.* **111** 145702
[34] Pototsky A and Stark H 2012 *EPL* **98** 50004
[35] Maggi C, Marconi U M B, Gnan N and Di Leonardo R 2015 *Sci. Rep.* **5** 10742
[36] Das S, Gompper G and Winkler R G 2018 *New J. Phys.* **20** 015001
[37] Volpe G and Volpe G 2013 *Am. J. Phys.* **81** 224
[38] Szamel G 2014 *Phys. Rev. E* **90** 012111
[39] Tailleur J and Cates M 2009 *EPL* **86** 60002
[40] Ye S, Liu P, Wei Z, Ye F, Yang M and Chen K 2020 *Chin. Phys. B* **29** 058201
[41] Tian W D , Gu Y, Guo Y K and Chen K 2017 *Chin. Phys. B* **26** 100502
[42] Howard M P, Gautam A, Panagiotopoulos A Z and Nikoubashman A 2016 *Phys. Rev. Fluids* **1** 044203
[43] Weeks J D, Chandler D and Andersen H C 1971 *J. Chem. Phys.* **54** 5237
[44] Plimpton S 1995 *J. Comput. Phys.* **117** 1
[45] Vicsek T, Czirók A, Ben-Jacob E, Cohen I and Shochet O 1995 *Phys. Rev. Lett.* **75** 1226
[46] Martens K, Angelani L, Di Leonardo R and Bocquet L 2012 *Eur. Phys. J. E.* **35** 84
[47] Ruiz-Franco J, Rovigatti L and Zaccarelli E 2018 *Eur. Phys. J. E.* **41** 80
[48] Espanol P and Warren P B 2017 *J. Chem. Phys.* **146** 150901